ROYAL SOCIETY
OF CHEMISTRY

PAPER

NiS₂ nanoparticles anchored on open carbon nanohelmets as an advanced anode for lithium-ion batteries†

D. D. Yang, M. Zhao, R. D. Zhang, Y. Zhang, C. C. Yang [ID] * and Q. Jiang [ID]

Low intrinsic conductivity and large volume expansion seriously restrict the efficient lithium storage performance of metal sulfides. Here, we fabricate a hybrid material of NiS₂ nanoparticles/carbon nanohelmets (NiS₂/CNHs) to address the above issues. As an anode material in lithium-ion batteries, NiS₂/CNHs exhibit excellent cycling stability (490 mA h g⁻¹ after 3000 cycles at 5 A g⁻¹) and rate properties (412 mA h g⁻¹ at 10 A g⁻¹), outperforming other NiSₓ-based anode materials. These remarkable performances originate from the three-dimensional helmet-like integrated architecture of NiS₂/CNHs, which reduces the electrode resistance due to the tight combination between NiS₂ and CNHs, provides efficient diffusion paths for the electrolyte and Li⁺ owing to the amorphous nanoporous carbon structure, and significantly mitigates the aggregation and buffers the large volumetric expansion of NiS₂ nanoparticles upon long-term cycling thanks to the open three-dimensional architecture and well-dispersed NiS₂ nanoparticles on it.

Introduction

Lithium-ion batteries (LIBs), as efficient energy storage devices, have been widely used in consumer electronics and electric vehicles due to their high energy density, light weight, long life span and environmental benignity.[1–5] In this context, developing advanced electrode materials with excellent electrochemical performance is of great importance to cater to the growing requirements of large-scale practical applications.[6–9] To date, a large number of LIB anode materials, such as carbonaceous materials,[10,11] alloys (NiSn, CuZn, SiCu, *etc.*),[12–14] metal oxides (Fe₂O₃, SnO₂, CoO₂, TiO₂, *etc.*),[15–18] and metal nitrides and sulfides (Ni₃N, Fe₃N, MoS₂, CoS₂, SnS₂, *etc.*),[19–23] have been extensively studied. Among the various candidates, transition metal sulfides (TMSs) have enormous potential due to their higher electronic conductivity, much better cycling performance and higher theoretical capacity than those of their metal oxide counterparts.[24] In particular, NiS₂ attracted many researchers' attention owing to its high theoretical capacity (870 mA h g⁻¹). Nevertheless, the inherent relatively low conductivity and huge volume change during the charge/discharge process restrict the electrochemical performance of NiS₂ in LIBs.[25,26]

To tackle the aforementioned issues, many effective strategies have been proposed to construct advanced NiS₂ nanostructures and their hybrid materials. In this regard, the hybridization of NiS₂ with carbon-based materials is an effective approach to improve the electrochemical properties.[25–27] For example, Chen *et al.* reported that a composite of NiS₂/graphene delivered a reversible capacity as high as 810 mA h g⁻¹ at a current density of 500 mA g⁻¹ after 1000 cycles.[26] Lou *et al.* synthesized a NiS₂@C hybrid material, which exhibits excellent rate performance and a reversible capacity of 577 mA h g⁻¹ at 2000 mA g⁻¹.[27] However, achieving both superior cycle stability and rate performance is highly desirable. Recently, Yang *et al.* synthesized a hybrid structure by anchoring NiO nanoparticles on open helmet-like carbon skeletons (NiO/CNHs), which shows both excellent long-term cycling performance (424 mA h g⁻¹ after 1500 cycles at 7.5C) and rate performance (450 mA h g⁻¹ at 15C).[28] Such a unique carbon nanoarchitecture is expected to also be applicable for NiS₂ nanoparticles.

Herein, a hybrid material of NiS₂ nanoparticles/carbon nanohelmets (NiS₂/CNHs) was fabricated through the sulfurization of NiO/CNHs. The NiS₂/CNH hybrid material has the following advantages: (1) the tight combination between NiS₂ nanoparticles and CNHs can greatly improve the overall conductivity of the hybrid material; (2) the CNH structure can be used as a matrix for dispersing NiS₂ nanoparticles uniformly, avoiding their self-aggregation and thus increasing the active sites for Li⁺ insertion/extraction; (3) the porous CNHs can provide efficient electrolyte pathways and accelerate carrier transfer; (4) the open CNH skeleton can effectively alleviate the internal stress caused by the large volume change of NiS₂

Key Laboratory of Automobile Materials (Jilin University), Ministry of Education, School of Materials Science and Engineering, Jilin University, Changchun 130022, China. E-mail: ccyang@jlu.edu.cn; Fax: +86-431-85095876; Tel: +86-431-85095371

† Electronic supplementary information (ESI) available. See DOI: 10.1039/c9na00661c

nanoparticles during the charge/discharge process. As expected, the NiS$_2$/CNH hybrid material exhibits superior rate performance (412 mA h g^{-1} at 10 A g^{-1}) and excellent long-term cycling stability (490 mA h g^{-1} after 3000 cycles at 5 A g^{-1}) as an ideal anode material in LIBs.

Results and discussion

Materials synthesis and characterization

The fabrication procedure of the NiS$_2$/CNH hybrid material is schematically illustrated in Fig. 1. The field-emission scanning electron microscope (FESEM) images of the corresponding products, including SiO$_2$ spheres, resorcinol and formaldehyde resin/SiO$_2$ spheres (RF/SiO$_2$), Ni(OH)$_2$/RF/SiO$_2$, NiO/C/SiO$_2$ and NiO/CNHs, are shown in Fig. S1–S5.† Firstly, RF resin shells were formed on the surface of the SiO$_2$ template spheres with a polymerization process. Then, Ni(OH)$_2$ was grown on the surface of RF/SiO$_2$ *via* a hydrothermal reaction followed by a pyrolysis treatment under nitrogen protection to obtain NiO/C/SiO$_2$. Afterwards, NiO/CNH hybrids were obtained through a template removal method in NaOH solution. Here, the formation mechanism of the CNHs can be described as follows. During the carbonization process, some gaseous products (CO$_2$, CO, H$_2$O, CH$_4$, H$_2$, *etc.*) were generated from the pyrolysis of RF, which escaped from the system once their pressure became high enough. The plasticity of the carbon shell was weakened due to the pressure impact and the large number of pores created by the release of gaseous products. During the etching process of SiO$_2$, the Si–O–C interconnections were destroyed, resulting in a decrease of the interfacial tension force. As a result, the shrinkage of carbon shells occurred under the influence of constrictive forces from NiO. With the continuous

increase of the shrinkage degree, it was difficult for the highly porous hollow carbon skeleton to withstand the shrinkage force, and it eventually fractured to form the CNH structure.[28] In addition, the intense agitation forces during the etching process also play an important role in accelerating the fracture of the hollow structure. Finally, NiO/CNHs were sulfurized with sublimed sulfur in a quartz tube reactor to obtain the NiS$_2$/CNH composite. It is known that Ni-based oxides and sulfides undergo conversion in LIBs. In general, TMSs exhibit higher electronic conductivity than their metal oxide counterparts.[24] Moreover, the metal–sulfur bonds in TMSs are relatively weaker than the metal–oxygen bonds in transition metal oxides (TMOs) due to the lower electronegativity of S compared with O, which is favorable for the conversion reaction for TMSs during the charge/discharge process in LIBs.[29,30] Note that the sulfurization process of NiO/CNHs was conducted under conditions of nitrogen protection, high sulfur content and high temperature. The corresponding conversion reaction from NiO to NiS$_2$ can be expressed using:

$$2NiO \text{ (s)} + 5S \text{ (g)} \rightarrow 2NiS_2 \text{ (s)} + SO_2 \text{ (g)}. \tag{1}$$
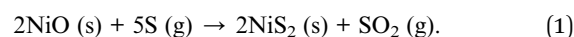
Such an approach has been reported in previous studies.[31,32] For example, Wu *et al.* synthesized a hybrid of NiS$_2$ nanosheets grown on a graphite substrate *via* the sulfidation of NiO nanosheets with S vapor at 350 °C under argon protection.[31] Li *et al.* reported that NiO hollow spheres were sulfurized to NiS$_2$ by using sulfur powder at 350 °C under an argon atmosphere.[32] For comparison, a sample of pristine NiS$_2$ was also fabricated by sulfurization of NiO without the CNH skeleton. All materials synthesis details are provided in the Experimental section (see the ESI† for details).

Fig. 2a compares the X-ray diffraction (XRD) patterns of NiS$_2$/CNHs and pristine NiS$_2$. For each sample, the characteristic peaks at 27.1°, 31.4°, 35.3°, 38.8°, 45.1° and 53.4° can be indexed to the (111), (200), (210), (211), (220) and (311) planes, respectively, of the cubic NiS$_2$ phase with the $Pa\bar{3}$ space group (JCPDF no. 89-7142). Moreover, for NiS$_2$/CNHs, the broad peak between 20° and 30° is assigned to the characteristic structure of amorphous carbon.[28,33] Fig. 2b shows the Raman spectrum of NiS$_2$/CNHs, in which two typical peaks at 1360 and 1586 cm^{-1} are assigned to the D band and G band of carbon, respectively.[34] The calculated value of I_D/I_G is 1.00, demonstrating the abundance of topological defects and disorders in CNHs, which are beneficial for lithium storage.[35] The nitrogen adsorption/desorption isotherm (see Fig. 2c) of NiS$_2$/CNHs exhibits a type-IV behavior with a representative hysteresis loop in the relative pressure range of 0.45–1 that can be linked to a large amount of mesopores in NiS$_2$/CNHs.[36,37] From the inset curve of Fig. 2c, the sizes of most pores are concentrated within 2–10 nm, while other pores exhibit a wide size distribution between 10 and 100 nm. Moreover, the NiS$_2$/CNHs exhibit a relatively large specific surface area of 96.62 m^2 g^{-1}. The large specific surface area and the high porosity result in a large electrode–electrolyte contact area and fast Li$^+$ transport, which are beneficial for high discharge capacity and excellent rate
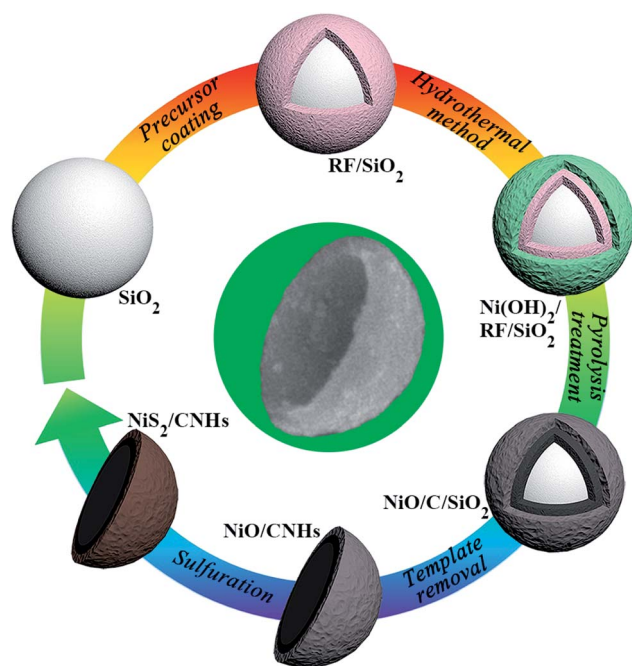

Fig. 1 Schematic illustration of the synthesis procedure of NiS$_2$/CNHs.
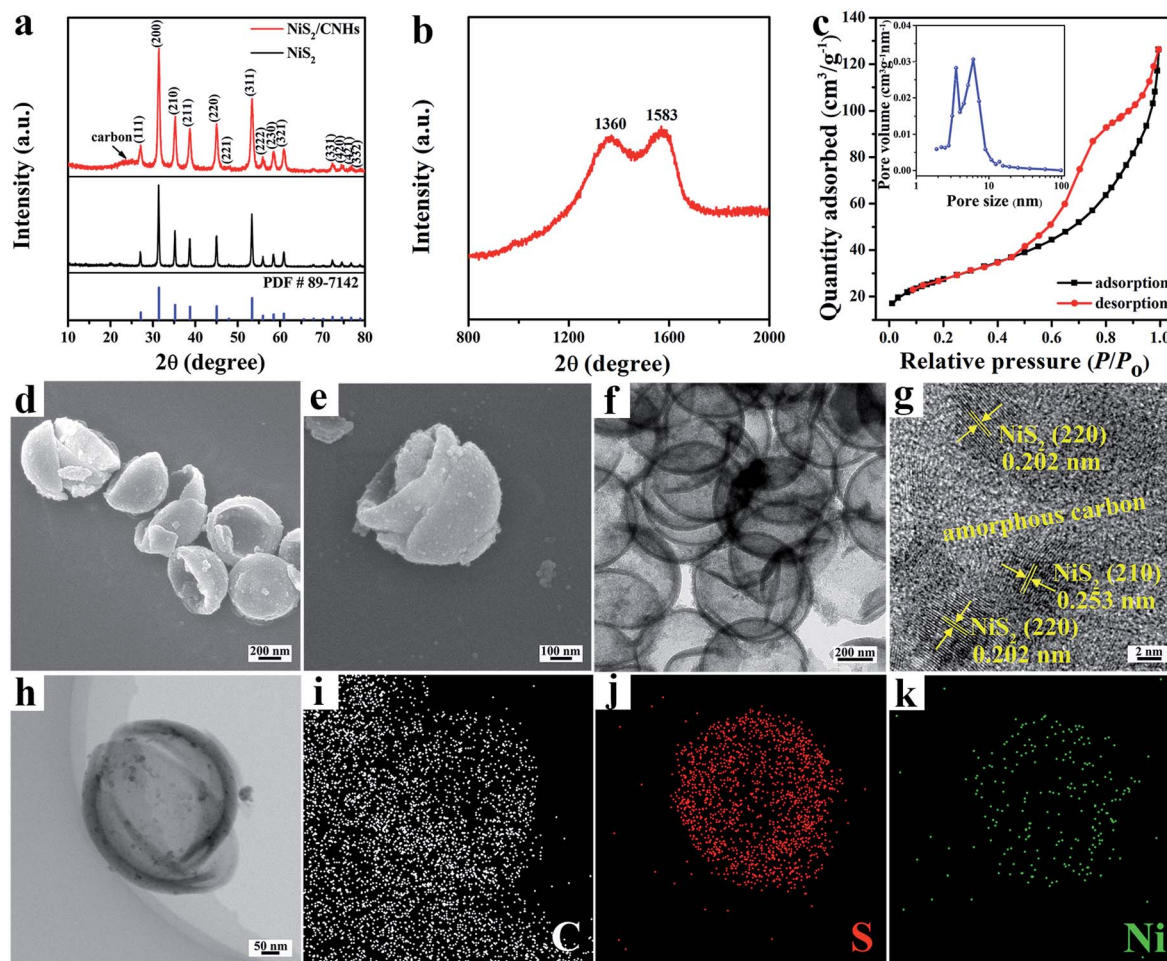
Fig. 2 Structural and morphological characterization. (a) XRD patterns of pristine NiS$_2$ and NiS$_2$/CNHs. (b) Raman spectrum of NiS$_2$/CNHs. (c) N$_2$ adsorption/desorption isotherms and pore size distribution (the inset) of NiS$_2$/CNHs. (d and e) FESEM images of NiS$_2$/CNHs at different magnifications. (f) TEM image of NiS$_2$/CNHs. (g) HRTEM image of NiS$_2$/CNHs. (h) TEM image of NiS$_2$/CNHs and corresponding elemental maps for (i) C, (j) S and (k) Ni elements.

performance.[38,39] Fig. 2d and e present the FESEM images of NiS$_2$/CNHs, where hollow CNHs are formed with heights of 200–300 nm and diameters of 400–600 nm. It is obvious that the NiS$_2$ nanoparticles are uniformly dispersed on CNHs without the accumulation of many nanoparticles. In contrast, the NiS$_2$ nanoparticles without CNHs as a carrier aggregated into a bulk one (see Fig. S6†), which demonstrates that CNHs can effectively inhibit the agglomeration of NiS$_2$ nanoparticles. Fig. 2f shows a transmission electron microscopy (TEM) image of NiS$_2$/CNHs, further confirming the uniform dispersion of NiS$_2$ nanoparticles on the CNH skeleton. Such an open structure can greatly alleviate the huge volume change of NiS$_2$ during the charge/discharge process and thus enhance the cycle stability of NiS$_2$/CNHs. It should be mentioned that the inner carbon layer in the open NiS$_2$/CNHs shows structural advantages for lithium storage by (i) providing a large number of active sites for Li$^+$ insertion/extraction, which is beneficial for the enhancement of the specific capacity; (ii) providing efficient diffusion paths for the electrolyte and Li$^+$; and (iii) significantly reducing the internal resistance contributed by the contact between NiS$_2$ and

the inner carbon layer. Fig. 2g presents a high-resolution TEM image of NiS$_2$/CNHs, in which the interplanar spacings of 0.202 nm and 0.253 nm correspond to the (220) and (210) planes of NiS$_2$, respectively. From the figure, NiS$_2$ nanoparticles are all surrounded by amorphous carbon, indicating the excellent contact between them. Fig. S7† exhibits a TEM image and particle size distribution (the inset) of NiS$_2$/CNHs, where the mean size of NiS$_2$ nanoparticles is 8.10 nm. Such small nanoparticles provide abundant active sites for Li$^+$ insertion/extraction, increasing the reversible capacity of the NiS$_2$/CNHs. Moreover, the TEM and elemental mapping images display homogeneous distributions of S and Ni along the CNH skeleton (see Fig. 2h–k). To further determine the content of active material in NiS$_2$/CNHs, a thermogravimetric analysis (TGA) test was carried out. As exhibited in Fig. S8,† the volatilization of water contained in the NiS$_2$/CNHs occurred below the temperature of 250 °C. The mass loss above 250 °C was ascribed to the oxidation of NiS$_2$ and carbon. Thus, the content of NiS$_2$ in the NiS$_2$/CNHs is calculated to be 83.8%, based on the equation in Fig. S8.†

The chemical composition and surface electronic state of C, S and Ni elements in NiS$_2$/CNHs were further investigated by X-ray photoelectron spectroscopy (XPS). The survey spectrum reveals that the primary elements in NiS$_2$/CNHs are C, S, Ni and O (see Fig. 3a). As presented in Fig. 3b, the high resolution XPS spectrum of C 1s has three obvious peaks, which correspond to the strong C–C bond (284.8 eV), C–O bond (285.5 eV) and weaker C=O bond (288.8 eV), respectively.[40,41] Five fitted peaks exist in the S 2p spectrum (see Fig. 3c) where the two strong peaks at 162.6 and 163.85 eV are attributed to 2p$_{3/2}$ and 2p$_{1/2}$ of the S element in the NiS$_2$, indicating the presence of S–S bonds in the NiS$_2$/CNHs. In addition, a pair of peaks around 163.55 eV and 164.7 eV are assigned to the residual S (α-S$_8$) in NiS$_2$/CNHs, which may be retained during the sulfurization process.[42,43] The peak located at 169.0 eV is ascribed to the S–O covalent bond due to the surface oxidation of the NiS$_2$/CNHs.[41,44] Note that elemental sulfur is not detected in the XRD pattern, indicating its trace amount.[45] Fig. 3d shows the high resolution XPS spectrum of Ni 2p, which exhibits three pairs of peaks. The peaks situated at 854.2 and 871.75 eV are attributed to 2p$_{3/2}$ and 2p$_{1/2}$ of Ni^{2+}, while the peaks located at 856.05 and 875.1 eV are assigned to 2p$_{3/2}$ and 2p$_{1/2}$ of Ni^{3+}. In addition, the two other peaks at 861.35 and 879.5 eV are ascribed to the satellite peaks of Ni 2p$_{3/2}$ and Ni 2p$_{1/2}$, respectively.[25,46]

Electrochemical performance

Fig. 4a presents the cyclic voltammetry (CV) curves of the NiS$_2$/CNH electrode for the initial five cycles within a voltage window of 0.01–3.0 V (vs. Li$^+$/Li) at a constant scan rate of 0.1 mV s^{-1}. During the first cathodic scan process, two strong peaks located at 1.50 V and 1.18 V are attributed to the intercalation of Li$^+$ into the NiS$_2$ lattice to form Li$_x$NiS$_2$ and the following conversion reaction process from Li$_x$NiS$_2$ to Ni and Li$_2$S, respectively.[26,27] It is noteworthy that the pronounced cathodic peak at 0.69 V, which disappears in the subsequent cycles, corresponds to the formation of an irreversible solid–electrolyte interface (SEI) layer.[26,27] Furthermore, a weak peak at 1.68 V can be attributed to the lithiation reaction of a trace amount of residual sulfur in the NiS$_2$/CNHs.[47] For the reverse anodic scan process, the part of lithium stored at the defects will be removed first, which generates a peak at about 1.16 V.[26] Two remarkable peaks at 2.01 V and 2.22 V are associated with the formation of Li$_x$NiS$_2$ and NiS$_2$, respectively.[25,27,48] The peak at 2.36 V, gradually weakened in the subsequent cycles, is ascribed to the conversion of Li$_2$S to S. Moreover, in the following cathodic sweep, the peak at 1.91 V and the extremely slight peaks nearby are attributed to the multi-step lithiation of S.[26] From the second cycle onward, the cathodic peaks at 1.50 V and 1.18 V slightly shift to 1.58 V and 1.27 V, respectively. Note that the CV profiles show little difference with increasing cycles from the third cycle, indicating the excellent cycling stability of the NiS$_2$/CNH electrode. According to previous studies,[26,27,48] the corresponding lithium storage conversion reactions can be expressed using the following equations:
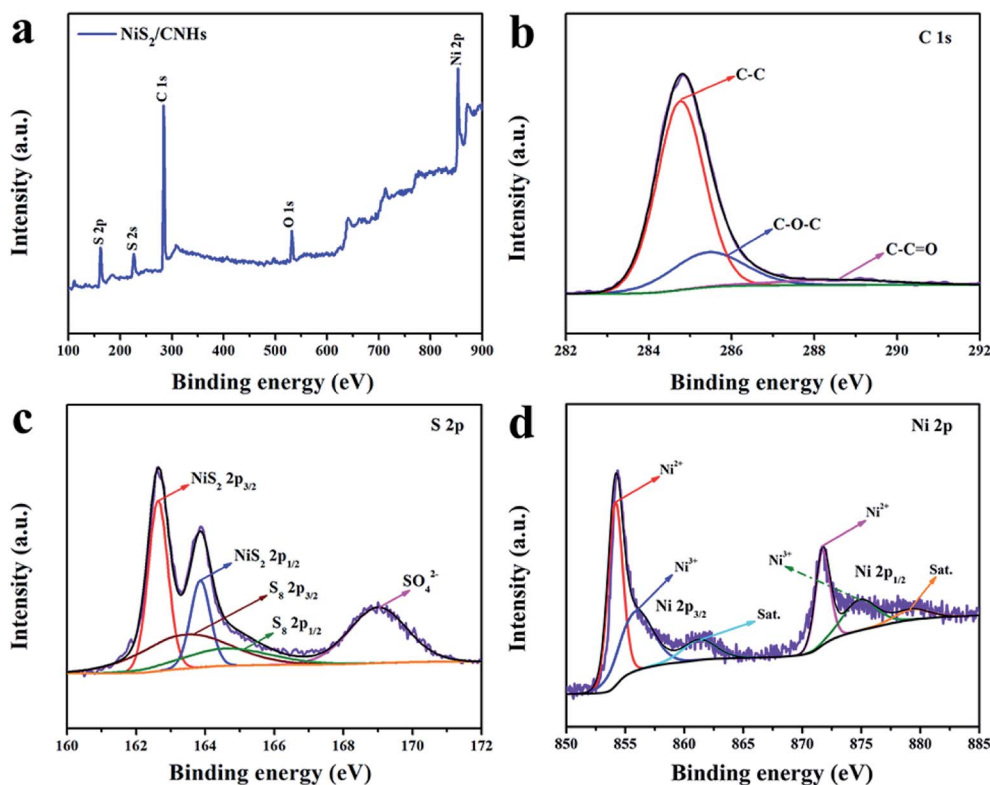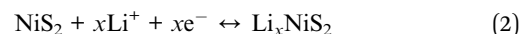
$$NiS_2 + xLi^+ + xe^- \leftrightarrow Li_xNiS_2 \tag{2}$$

Fig. 3 XPS analysis. (a) The survey XPS spectrum of NiS$_2$/CNHs. (b–d) High-resolution XPS spectra of C 1s, S 2p and Ni 2p, respectively, of NiS$_2$/CNHs.
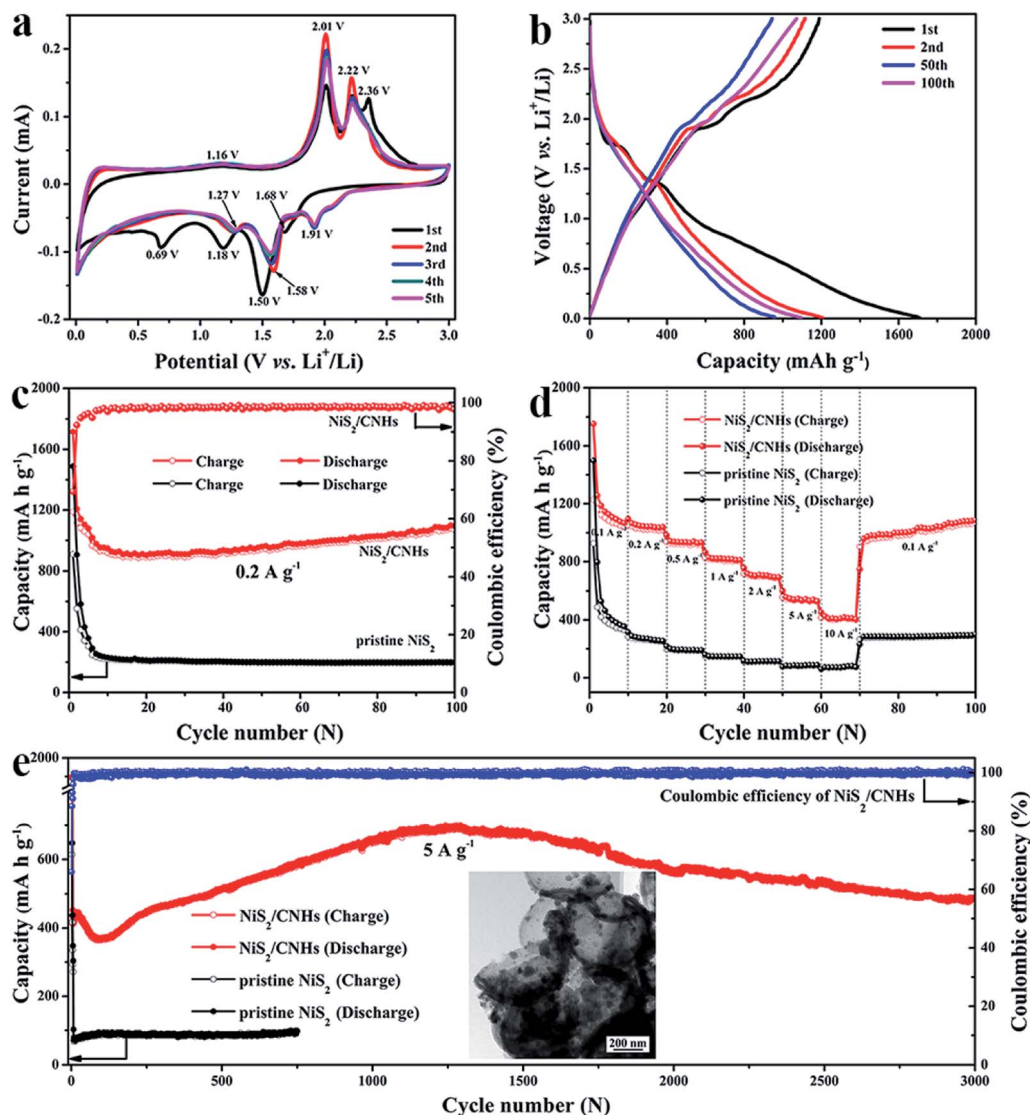
Fig. 4 Electrochemical performances of the NiS$_2$/CNH electrode in LIBs. (a) CV curves of the NiS$_2$/CNH electrode at a scan rate of 0.1 mV s^{-1}. (b) Galvanostatic discharge/charge curves of the NiS$_2$/CNH electrode at a current density of 0.2 A g^{-1}. (c) Cycling performance and coulombic efficiency of the pristine NiS$_2$ and NiS$_2$/CNH electrodes at a current density of 0.2 A g^{-1}. (d) Rate performance of the pristine NiS$_2$ and NiS$_2$/CNH electrodes at different current densities. (e) Long-term cycling performance and coulombic efficiency of the pristine NiS$_2$ and NiS$_2$/CNH electrodes at a current density of 5 A g^{-1} and the TEM image after 2000 cycles (the inset).

$$Li_xNiS_2 + (4-x)Li^+ + (4-x)e^- \leftrightarrow Ni + 2Li_2S. \quad (3)$$
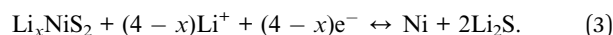
The galvanostatic charge/discharge profiles of the NiS$_2$/CNH electrode for the 1st, 2nd, 50th and 100th cycles at a current density of 0.2 A g^{-1} are shown in Fig. 4b. The NiS$_2$/CNH electrode delivers high first-cycle discharge and charge capacities of 1714.5 and 1189.2 mA h g^{-1}, respectively, with an initial coulombic efficiency of 69.36%. The high irreversible capacity loss during the first cycle can be attributed to the formation of the SEI layer.[49–52] The inconspicuous voltage plateaus in Fig. 4b may be attributed to the complicated multi-step reactions of NiS$_2$, the pseudocapacitive behavior of nanosized-NiS$_2$ particles, and the partial effect from the sloping voltage curve of carbonaceous material.[53–57] Such a phenomenon has also been

reported for various TMS anode materials in previous studies.[27,51,58] In this work, the NiS$_2$/CNH electrode material exhibits high specific capacity and excellent cycling stability and rate performance. In addition, most of the charge capacity is released below a voltage of 1.5 V, which is beneficial to improving the energy density of batteries.[59,60] Thus, the NiS$_2$/CNH hybrid has great potential for application in high-performance LIBs in the near future. Note that the active material is the NiS$_2$/CNH hybrid and all the capacities recorded in this work are calculated on the basis of the total mass of NiS$_2$/CNHs. The cycling performances of NiS$_2$/CNH and pristine NiS$_2$ electrodes at a current density of 0.2 A g^{-1} are shown in Fig. 4c. The NiS$_2$/CNH hybrid electrode exhibits an excellent cycling performance with a specific capacity of 1096 mA h g^{-1} after 100 cycles, which is much higher than that of the pristine NiS$_2$

electrode (only 199 mA h g^{-1}). Moreover, the coulombic efficiency of the NiS$_2$/CNH electrode is close to 100%, indicating its excellent reversibility during the Li$^+$ insertion/extraction process. The discharge capacity of the NiS$_2$/CNH electrode drops from 1714.5 mA h g^{-1} to 902.2 mA h g^{-1} in the first 20 cycles and then increases gradually to a value as high as 1096 mA h g^{-1} after 100 cycles. To the best of our knowledge, this phenomenon of capacity increase is common in metal oxide/sulfide composites and is normally ascribed to the improved charge transfer kinetics by the reversible reaction between metal nanoparticles and electrolytes and the gradual activation process during the cycling process.[51,61] However, it is apparent that the capacity retention for the pristine NiS$_2$ electrode is very poor and shows a monotonous decreasing trend. Fig. 4d compares the rate performance of the NiS$_2$/CNH and pristine NiS$_2$ electrodes. The excellent rate performance of NiS$_2$/CNHs is evidenced by the average specific capacities of 1112, 1045, 935, 819, 706, 541 and 412 mA h g^{-1} at current densities of 0.1, 0.2, 0.5, 1, 2, 5 and 10 A g^{-1}, respectively. Moreover, the reversible capacity of the NiS$_2$/CNH electrode rapidly recovers to 1087.1 mA h g^{-1} in the 30th cycle when the current density is changed back to 0.1 A g^{-1} and then maintains a continuous increase during further cycling, while the pristine NiS$_2$ electrode shows a much worse performance at each current density. The superior rate performance of NiS$_2$/CNHs is attributed to the low internal resistance, which has been demonstrated by the electrochemical impedance spectroscopy (EIS) measurement results shown in Fig. S9.† The NiS$_2$/CNH electrode displays a smaller intrinsic electrode/electrolyte resistance R_{el} (=1.9 Ω) and charge transfer resistance R_{ct} (=57 Ω) than the pristine NiS$_2$ electrode (2.5 Ω and 143 Ω, respectively). In addition, the large specific surface area and pore volume of NiS$_2$/CNHs provide efficient diffusion pathways for Li$^+$ and the electrolyte, which is also beneficial for achieving excellent rate performance. Furthermore, Fig. S10† displays the comparison of the rate performance between the NiS$_2$/CNH electrode in this work and previously reported NiS$_x$-based anode materials. It is obvious that NiS$_2$/CNHs show the best rate performance among them.

To evaluate the long-term cycling stability of the NiS$_2$/CNH electrode, it was galvanostatically discharged and charged at 0.1 A g^{-1} for the first five cycles and then at 5 A g^{-1} for 3000 cycles. The corresponding results are shown in Fig. 4e. The hybrid electrode suffers from capacity fluctuations during long-term cycling. After the first 100 cycles, the specific capacity of the hybrid electrode drops from 1790 mA h g^{-1} to 370 mA h g^{-1}, resulting from the formation of the SEI film and irreversible transformation from NiS$_2$ to metallic Ni nanoparticles.[28,62] Then, the specific capacity increases gradually to the maximum capacity (699.4 mA h g^{-1}) in the 1292nd cycle. Such a capacity increase can be attributed to the improved charge transfer kinetics during the gradual activation process and reversible reaction between Ni nanoparticles and electrolytes. This phenomenon has also been observed in other composites of TMOs/TMSs and carbon.[51,63,64] In addition, electrochemical impedance spectroscopy (EIS) of the NiS$_2$/CNH electrode after the 100th and 350th cycles was performed and the corresponding results are shown in Fig. S11.† It is

found that the electrode/electrolyte resistance R_{el} (=3.2 Ω) and charge transfer resistance R_{ct} (=34.3 Ω) values in the 350th cycle are smaller than those in the 100th cycle (R_{el} = 3.7 Ω and R_{ct} = 44.7 Ω). Note that the impedance decreases gradually with the increasing cycles and the R_{ct} values after cycling are lower than that of the fresh cell (R_{ct} = 57 Ω). This phenomenon should be attributed to the *in situ* generated Ni from the incomplete conversion reactions which could enhance the electronic conductivity of the electrode.[28,64] As shown in Fig. S11,† there exist two semicircles in the high-frequency region, suggesting the formation of a new phase (Ni nanoparticles), which is also consistent with the above analysis results.[28,65] Finally, the specific capacity decreases gradually to 490 mA h g^{-1} after 3000 cycles. This may be ascribed to the falling off of some active materials caused by the volume expansion during the long-term continuous charge/discharge process.[50] In contrast, the specific capacity of the pristine NiS$_2$ electrode is only 97.6 mA h g^{-1} after 750 cycles. As exhibited in the inset TEM image in Fig. 4e, the NiS$_2$/CNH hybrid retains its original helmet-like skeleton after 2000 cycles, which indicates its excellent structural stability. Besides, Fig. S12† shows a FESEM image of the NiS$_2$/CNH electrode after 2000 cycles, further demonstrating the good integrity of the electrode material after long-term cycling.

As listed in Table S1,† the NiS$_2$/CNH electrode exhibits the best cycling stability and rate performance among currently reported NiS$_x$-based anode materials.[24-26,39,46,48,49,66-68] The excellent electrochemical performance of NiS$_2$/CNHs can be attributed to their characteristic structure with the following advantages: (1) well-dispersed NiS$_2$ nanoparticles on CNHs can effectively mitigate the aggregation and buffer the volumetric expansion of NiS$_2$ nanoparticles upon long-term cycling; (2) the tight combination between NiS$_2$ nanoparticles and CNHs can greatly improve the overall conductivity of the NiS$_2$/CNH electrode; and (3) the three-dimensional nanoporous carbon architecture can provide efficient diffusion paths for the electrolyte and Li$^+$ to fully come into contact with electrochemically active NiS$_2$ nanoparticles.

Conclusion

In summary, we have successfully fabricated a hybrid material of NiS$_2$/CNHs, which combines the advantages of the high conductivity and good stability of the carbon material and the high theoretical capacity of NiS$_2$. Benefiting from the above superior properties, when tested as an anode in LIBs, the NiS$_2$/CNH electrode exhibits superior rate performance (412 mA h g^{-1} at 10 A g^{-1}) and excellent cycling stability (490 mA h g^{-1} after 3000 cycles at 5 A g^{-1}), outperforming other NiS$_x$-based materials and making it a promising candidate as an anode material for highly reversible lithium storage.

Conflicts of interest

There are no conflicts to declare.

Acknowledgements

References

1 D. Larcher and J.-M. Tarascon, *Nat. Chem.*, 2015, **7**, 19–29.

2 Y.-M. Chiang, *Science*, 2010, **330**, 1485–1486.

3 B. Dunn, H. Kamath and J.-M. Tarascon, *Science*, 2011, **334**, 928–935.

4 X. Hu, J. Jia, G. Wang, J. Chen, H. Zhan and Z. Wen, *Adv. Energy Mater.*, 2018, **8**, 1801452.

5 X. Su, Q. Wu, J. Li, X. Xiao, A. Lott, W. Lu, B. W. Sheldon and J. Wu, *Adv. Energy Mater.*, 2014, **4**, 1300882.

6 Y. Zhao, L. P. Wang, M. T. Sougrati, Z. Feng, Y. Leconte, A. Fisher, M. Srinivasan and Z. Xu, *Adv. Energy Mater.*, 2017, **7**, 1601424.

7 X. Feng, M. Ouyang, X. Liu, L. Lu, Y. Xia and X. He, *Energy Storage Materials*, 2018, **10**, 246–267.

8 X. Hu, Y. Li, G. Zeng, J. Jia, H. Zhan and Z. Wen, *ACS Nano*, 2018, **12**, 1592–1602.

9 J. Xu, F. Lin, M. M. Doeff and W. Tong, *J. Mater. Chem. A*, 2017, **5**, 874–901.

10 L. Qie, W.-M. Chen, Z.-H. Wang, Q.-G. Shao, X. Li, L.-X. Yuan, X.-L. Hu, W.-X. Zhang and Y.-H. Huang, *Adv. Mater.*, 2012, **24**, 2047–2050.

11 X. Liu, D. Chao, Y. Li, J. Hao, X. Liu, J. Zhao, J. Lin, H. J. Fan and Z. X. Shen, *Nano Energy*, 2015, **17**, 43–51.

12 J. Hassoun, S. Panero, P. Simon, P. L. Taberna and B. Scrosati, *Adv. Mater.*, 2007, **19**, 1632–1635.

13 A. Varzi, L. Mattarozzi, S. Cattarin, P. Guerriero and S. Passerini, *Adv. Energy Mater.*, 2018, **8**, 1701706.

14 H. Song, H. X. Wang, Z. Lin, X. Jiang, L. Yu, J. Xu, Z. Yu, X. Zhang, Y. Liu, P. He, L. Pan, Y. Shi, H. Zhou and K. Chen, *Adv. Funct. Mater.*, 2016, **26**, 524–531.

15 B. Wang, J. S. Chen, H. B. Wu, Z. Wang and X. W. Lou, *J. Am. Chem. Soc.*, 2011, **133**, 17146–17148.

16 X. W. Lou, Y. Wang, C. Yuan, J. Y. Lee and L. A. Archer, *Adv. Mater.*, 2006, **18**, 2325–2329.

17 S. Zhu, J. Li, X. Deng, C. He, E. Liu, F. He, C. Shi and N. Zhao, *Adv. Funct. Mater.*, 2017, **27**, 1605017.

18 Z. Wang and X. W. Lou, *Adv. Mater.*, 2012, **24**, 4124.

19 C. Chen, X. Xie, B. Anasori, A. Sarycheva, T. Makaryan, M. Zhao, P. Urbankowski, L. Miao, J. Jiang and Y. Gogotsi, *Angew. Chem., Int. Ed.*, 2018, **57**, 1846–1850.

20 L. Yu, J. F. Yang and X. W. Lou, *Angew. Chem., Int. Ed.*, 2016, **55**, 1–5.

21 J. Seo, J. Jang, S. Park, C. Kim, B. Park and J. Cheon, *Adv. Mater.*, 2008, **20**, 4269–4273.

22 M.-S. Balogun, Y. Zeng, W. Qiu, Y. Luo, A. Onasanya, T. K. Olaniyi and Y. Tong, *J. Mater. Chem. A*, 2016, **4**, 9844–9849.

23 H. Huang, S. Gao, A.-M. Wu, K. Cheng, X.-N. Li, X.-X. Gao, J.-J. Zhao, X.-L. Dong and G.-Z. Cao, *Nano Energy*, 2017, **31**, 74–83.

24 Z. Gao, N. Song, Y. Zhang and X. Li, *Nano Lett.*, 2015, **15**, 8194–8203.

25 Y. Zhang, F. Lu, L. Pan, Y. Xu, Y. Yang, Y. Bando, D. Golberg, J. Yao and X. Wang, *J. Mater. Chem. A*, 2018, **6**, 11978–11984.

26 Q. Chen, W. Chen, J. Ye, Z. Wang and J. Y. Lee, *J. Power Sources*, 2015, **294**, 51–58.

27 P. Lou, Y. Tan, P. Lu, Z. Cui and X. Guo, *J. Mater. Chem. A*, 2016, **4**, 16849–16855.

28 C. C. Yang, W. T. Jing, C. Li and Q. Jiang, *J. Mater. Chem. A*, 2018, **6**, 3877–3883.

29 X. Hu, Y. Liu, J. Chen, J. Jia, H. Zhan and Z. Wen, *J. Mater. Chem. A*, 2019, **7**, 1138–1148.

30 Y. Xiao, S. H. Lee and Y.-K. Sun, *Adv. Energy Mater.*, 2017, **7**, 1601329.

31 X. Wu, B. Yang, Z. Li, L. Lei and X. Zhang, *RSC Adv.*, 2015, **5**, 32976–32982.

32 D. Li, X. Zhao, R. Yu, B. Wang, H. Wang and D. Wang, *Inorg. Chem. Front.*, 2018, **5**, 535–540.

33 C. C. Yang, D. M. Zhang, L. Du and Q. Jiang, *J. Mater. Chem. A*, 2018, **6**, 12663–12671.

34 R. Bi, C. Zeng, H. Huang, X. Wang and L. Zhang, *J. Mater. Chem. A*, 2018, **6**, 14077–14082.

35 H.-G. Wang, Y. Wang, Y. Li, Y. Wan and Q. Duan, *Carbon*, 2015, **82**, 116–123.

36 J. Li, D. Yan, X. Zhang, S. Hou, T. Lu, Y. Yao and L. Pan, *J. Mater. Chem. A*, 2017, **5**, 20428–20438.

37 W. T. Jing, Y. Zhang, Y. Gu, Y. F. Zhu, C. C. Yang and Q. Jiang, *Matter*, 2019, **1**, 720–733.

38 C. Li, M. Zhao, C. N. Sun, B. Jin, C. C. Yang and Q. Jiang, *J. Power Sources*, 2018, **397**, 162–169.

39 A. A. AbdelHamid, X. Yang, J. Yang, X. Chen and J. Y. Ying, *Nano Energy*, 2016, **26**, 425–437.

40 W. Zhao, S. Ci, X. Hu, J. Chen and Z. Wen, *Nanoscale*, 2019, **11**, 4688–4695.

41 T. Tian, L. Huang, L. Ai and J. Jiang, *J. Mater. Chem. A*, 2017, **5**, 20985–20992.

42 Q. Chen, S. Sun, T. Zhai, M. Yang, X. Zhao and H. Xia, *Adv. Energy Mater.*, 2018, **8**, 1800054.

43 Y. Lu, X. Li, J. Liang, L. Hu, Y. Zhu and Y. Qian, *Nanoscale*, 2016, **8**, 17616–17622.

44 K. Liang, K. Marcus, S. Zhang, L. Zhou, Y. Li, S. T. D. Oliveira, N. Orlovskaya, Y.-H. Sohn and Y. Yang, *Adv. Energy Mater.*, 2017, **7**, 1701309.

45 G. Zhao, Y. Zhang, L. Yang, Y. Jiang, Y. Zhang, W. Hong, Y. Tian, H. Zhao, J. Hu, L. Zhou, H. Hou, X. Ji and L. Mai, *Adv. Funct. Mater.*, 2018, **28**, 1803690.

46 Y. Lin, Z. Qiu, D. Li, S. Ullah, Y. Hai, H. Xin, W. Liao, B. Yang, H. Fan, J. Xu and C. Zhu, *Energy Storage Materials*, 2018, **11**, 67–74.

47 J. Ruan, T. Yuan, Y. Pang, S. Luo, C. Peng, J. Yang and S. Zheng, *Carbon*, 2018, **126**, 9–16.

48 W. Pi, T. Mei, J. Li, J. Wang, J. Li and X. Wang, *Chem. Eng. J.*, 2018, **335**, 275–281.

49 J. Zhu, Y. Li, S. Kang, X.-L. Wei and P. K. Shen, *J. Mater. Chem. A*, 2014, **2**, 3142–3147.

50 P. Fan, H. Liu, L. Liao, J. Fu, Z. Wang, G. Lv, L. Mei, H. Hao, J. Xing and J. Dong, *RSC Adv.*, 2017, **7**, 49739–49744.

51 R. Wu, D. Wang, X. Rui, B. Liu, K. Zhou, A. W. K. Law, Q. Yan, J. Wei and Z. Chen, *Adv. Mater.*, 2015, **27**, 3038–3044.

52 H. Li, X. Wang, Z. Zhao, Z. Tian, D. Zhang and Y. Wu, *ChemElectroChem*, 2019, **6**, 404–412.

53 Y. F. Yuan, L. W. Ye, D. Zhang, F. Chen, M. Zhu, L. N. Wang, S. M. Yin, G. S. Cai and S. Y. Guo, *Electrochim. Acta*, 2019, **299**, 289–297.

54 H.-S. Kim, J. B. Cook, S. H. Tolbert and B. Dunn, *J. Electrochem. Soc.*, 2015, **162**, 5083–5090.

55 V. Augustyn, P. Simonbc and B. Dunn, *Energy Environ. Sci.*, 2014, **7**, 1597–1614.

56 Y. Chen, X. Li, K. Park, J. Song, J. Hong, L. Zhou, Y.-W. Mai, H. Huang and J. B. Goodenough, *J. Am. Chem. Soc.*, 2013, **135**, 16280–16283.

57 Q. Pan, J. Xie, S. Liu, G. Cao, T. Zhu and X. Zhao, *RSC Adv.*, 2013, **3**, 3899–3906.

58 H. Jiang, D. Ren, H. Wang, Y. Hu, S. Guo, H. Yuan, P. Hu, L. Zhang and C. Li, *Adv. Mater.*, 2015, **27**, 3687–3695.

59 C. Wu, P. Kopold, P. A. van Aken, J. Maier and Y. Yu, *Adv. Mater.*, 2017, **29**, 1604015.

60 L. Xiao, Y. Cao, W. A. Henderson, M. L. Sushko, Y. Shao, J. Xiao, W. Wang, M. H. Engelhard, Z. Nie and J. Liu, *Nano Energy*, 2016, **19**, 279–288.

61 Y. Du, Z. Yin, J. Zhu, X. Huang, X.-J. Wu, Z. Zeng, Q. Yan and H. Zhang, *Nat. Commun.*, 2012, **3**, 1177.

62 C. Peng, B. Chen, Y. Qin, S. Yang, C. Li, Y. Zuo, S. Liu and J. Yang, *ACS Nano*, 2012, **6**, 1074–1081.

63 H. Li, Y. Su, W. Sun and Y. Wang, *Adv. Funct. Mater.*, 2016, **26**, 8345–8353.

64 J. Luo, J. Liu, Z. Zeng, C. F. Ng, L. Ma, H. Zhang, J. Lin, Z. Shen and H. J. Fan, *Nano Lett.*, 2013, **13**, 6136–6143.

65 S. Venkatachalam, H. Zhu, C. Masarapu, K. Hung, Z. Liu, K. Suenaga and B. Wei, *ACS Nano*, 2009, **3**, 2177–2184.

66 X. Wang, X. Liu, G. Wang, Y. Zhou and H. Wang, *J. Power Sources*, 2017, **342**, 105–115.

67 L. Zhang, Y. Huang, Y. Zhang, H. Gu, W. Fan and T. Liu, *Adv. Mater. Interfaces*, 2016, **3**, 1500467.

68 X. Wu, S. Li, Y. Xu, B. Wang, J. Liu and M. Yu, *Chem. Eng. J.*, 2019, **356**, 245–254.